Mon. Not. R. Astron. Soc. **000**, 1–19 (2010) Printed 30 March 2010 (MN LATEX style file v2.2)

Empirical calibrations of optical absorption line indices based on the stellar library MILES

Jonas Johansson, Daniel Thomas and Claudia Maraston
Institute of Cosmology and Gravitation, Dennis Sciama Building, Burnaby Road, Portsmouth PO1 3FX

30 March 2010

ABSTRACT

Stellar population models of absorption line indices are an important tool for the analysis of stellar population spectra. They are most accurately modelled through empirical calibrations of absorption line indices with the stellar parameters effective temperature, metallicity, and surface gravity, the so-called fitting functions. Here we present new empirical fitting functions for the 25 optical Lick absorption line indices based on the new stellar library MILES. The major improvements with respect to the Lick/IDS library are the better sampling of stellar parameter space, a generally higher signal- to-noise, and a careful flux calibration. In fact we find that errors on individual index measurements in MILES are considerably smaller than in Lick/IDS. Instead we find the rms of the residuals between the final fitting functions and the data to be dominated by errors in the stellar parameters. We provide fitting functions for both Lick/IDS and MILES spectral resolutions, and compare our results with other fitting functions in the literature. A Fortran 90 code is available online in order to simplify the implementation in stellar population models. We further calculate the offsets in index measurements between the Lick/IDS system to a flux calibrated system. For this purpose we use the three libraries MILES, ELODIE, and STELIB. We find that offsets are negligible in some cases, most notably for the widely used indices Hβ, Mgb, Fe5270, and Fe5335. In a number of cases, however, the difference between flux calibrated library and Lick/IDS is significant with the offsets depending on index strengths. Interestingly, there is no general agreement between the three libraries for a large number of indices, which hampers the derivation of a universal offset between the Lick/IDS and flux calibrated systems.

Key words: line: profiles – stars: abundances – stars: fundamental parameters

1 INTRODUCTION

Stellar population models of absorption line indices are a key tool for the analysis of star cluster and galaxy absorption spectra. They are used to derive the fundamental stellar population properties such as age, metallicity and element abundance ratios. In particular, optical absorption line diagnostics in the spectra of evolved stellar populations have successfully been adopted in the past in studies on galaxy evolution (e.g. Worthey, Faber & Gonzalez 1992; Davies, Sadler & Peletier 1993; Vazdekis et al. 1997; Kuntschner & Davies 1998; Worthey 1998; Trager et al. 1998; Henry & Worthey 1999; Kuntschner 2000; Trager et al. 2000; Thomas et al. 2005) and globular cluster formation (e.g. Kissler-Patig 1998; Forbes et al. 2001; Kuntschner 2002; Brodie et al. 2005; Puzia et al. 2005). The Lick/IDS system (Burstein et al. 1984; Faber et al. 1985; Gorgas et al. 1993; Worthey et al. 1994; Worthey & Ottaviani 1997; Trager et al. 1998) is the standard set of absorption line indices that has been used extensively during the last two decades for studying absorption features of stellar populations. This system consists of index definitions for 25 prominent absorption features between 4000 and 6500 Å present in the spectra of evolved stellar populations.

For studies of galaxy and star cluster evolution, absorption lines need to be modelled for stellar populations (e.g. Maraston 1998, 2005; Bruzual & Charlot 2003; Vazdekis 1999; Leitherer et al. 1999; Worthey et al. 1994; Worthey & Ottaviani 1997; Rose et al. 1994; Trager et al. 2000; Thomas, Maraston & Bender 2003; Thomas, Maraston & Korn 2004). A convenient way goes through the use of empirical calibrations. This is motivated by the fact that theoretical model atmospheres are known to suffer from incomplete line lists and continuum uncertainties. (e.g. Korn, Maraston & Thomas 2005; Coelho et al. 2007; Rodríguez-Merino et al. 2005; Lee, Worthey & Dotter 2009; Walcher et al. 2009). Empirical calibrations on the

other hand have the disadvantage to be hardwired to the chemical abundance pattern of the Milky Way, which can be overcome in a semi-empirical approach as in the models by Trager et al. (2000), Thomas et al. (2003, 2004) and Schiavon (2007)

Empirical calibrations can be inserted in the models in two ways. In the first and most widely used approach, absorption line indices enter stellar population modelling through calibrations of the empirical relationship between the indices and the stellar atmospheric parameters $T_{\rm eff}$, $\log g$ and [Fe/H] as provided by stellar libraries. As these calibrations are usually obtained through polynomial fitting procedures they are commonly referred to as 'fitting functions'. The quality of the final stellar population model critically depends on the accuracy with which these relationships can be inferred from stellar libraries, i.e. the coverage of stellar parameter space and the reliability of the index measurements. The computational procedure with which the fitting functions are determined is a further crucial step in producing accurate models. A number of studies in the literature are devoted to such empirical calibrations for various stellar libraries, either for the Lick indices, parts of the Lick indices or other prominent absorption features (Buzzoni, Gariboldi & Mantegazza 1992; Buzzoni, Mantegazza & Gariboldi 1994; Worthey et al. 1994; Borges et al. 1995; Gorgas et al. 1999; Cenarro et al. 2002; Schiavon 2007; Maraston et al. 2009).

Alternatively to the use of fitting functions, absorption line indices can be measured directly on the synthetic spectral energy distribution (SED) from stellar population models that are based on empirical stellar libraries. The benefit of this method is that the full SED can be compared pixel-by-pixel to observations (e.g. Panter et al. 2007; Tojeiro et al. 2007).

The major strength of fitting functions, instead, lies in the fact that they allow for interpolation between well populated regions of stellar parameter space which increases the accuracy of the model in stellar parameter space that is only sparsely sampled by empirical stellar libraries. Moreover, each absorption index or spectral feature is represented by an individual fitting function, which is optimised to best reproduce its behaviour in stellar parameter space. Fitting functions are also easier to implement in a stellar population synthesis code, and models based on fitting functions are better comparable.

The widely used fitting functions of Worthey et al. (1994) and Worthey & Ottaviani (1997) are based on the Lick/IDS stellar library (Burstein et al. 1984; Faber et al. 1985). They are adopted in most stellar population models (Worthey 1994; Vazdekis et al. 1996; Trager et al. 2000; Thomas et al. 2003, 2004, 2005; Annibali et al. 2007) in the literature. Other fitting functions based on the same stellar library exist (Buzzoni et al. 1992, 1994; Borges et al. 1995) and lead to overall consistent results in the final stellar population model (Maraston et al. 2003). Major progress has been made with the advent of a new generation of stellar libraries (Jones 1999; Prugniel & Soubiran 2001; Le Borgne et al. 2003; Sánchez-Blázquez et al. 2006) that have led to considerable improvements regarding coverage of stellar parameter space, spectral resolution, signal-to-noise ratio, and flux calibration.

In particular the latter is a critical step forward. As the Lick/IDS system is not flux calibrated, observations have to be re-calibrated onto the Lick/IDS system through comparison with Lick standard stars. This requirement hampers the analysis of data samples for which spectra of such calibration stars are either not available at sufficient quality or do not cover the appropriate rest-frame wavelength range. This problem is most imminent in high redshift observations and in galaxy redshift surveys such as the Sloan Digital Sky Survey (York et al. 2000). The new flux calibrated libraries allow the analysis of flux calibrated spectra at any redshift without spectroscopic standard stars.

Flux-calibrated stellar libraries in the literature that are suitable for stellar population modelling include the *Jones* (Jones 1999), *ELODIE* (Prugniel & Soubiran 2001), *STELIB* (Le Borgne et al. 2003) and *MILES* (Sánchez-Blázquez et al. 2006) libraries. The *MILES* library is particularly well suited for stellar population modelling of absorption line indices owing to its favourable combination of spectral resolution, wavelength range, stellar parameter coverage, and quality of flux calibration. In this paper we present new Lick index fitting functions based on the *MILES* stellar library. To take advantage of the full spectral resolution of the *MILES* library we have produced fitting functions for both the lower Lick/IDS resolution ($8-11$ Å FWHM) and the higher resolution of the *MILES* library (2.3 Å FWHM). A new version of the TMB stellar population model of absorption line indices based on these new fitting functions will be presented in a subsequent paper.

This paper is organized as follows. In Section 2 we present the Lick indices measured on the *MILES* library and a quality evaluation of the index measurements. We discuss offsets between the flux calibrated MILES and the Lick/IDS systems. The empirical fitting method is presented in Section 3 along with the resulting fitting functions. In Section 4 we compare the fitting functions of this work with fitting functions from the literature. We summarise in Section 5.

2 THE *MILES* STELLAR LIBRARY

The *MILES* library (Sánchez-Blázquez et al. 2006) consists of 985 stars with spectra in a wavelength range of 3525-7500 Å, well covering the Lick indices, and with a spectral resolution of 2.3 Å (see Sánchez-Blázquez et al. 2006 for further details). Important for the aim of this work is the careful flux-calibration of the *MILES* spectra. Also, Sánchez-Blázquez et al. (2006) selected the sample of stars to fill the gaps in stellar parameter space covered by previous stellar libraries. This makes the *MILES* library particularly suitable for modelling absorption line indices of stellar populations.

Stellar parameter estimates in the literature show a scatter due to varying methods applied, as discussed in Maraston et al. (2003) for [Fe/H]. The stellar parameters ($T_{\rm eff}$, $\log g$ or [Fe/H]) for the stars in the *MILES* library are presented in Cenarro et al. (2007), where estimates from the literature have been used and put on a homogeneous scale. 3 of 985 stars have no available estimates for none of the stellar parameters $T_{\rm eff}$, $\log g$ or [Fe/H]. 35 stars lack estimates only for [Fe/H] and are located in sparsely populated regions at the ends of the $T_{\rm eff}$ range. The stars have therefore been

Table 1. Typical Lick index errors and offsets to the Lick/IDS library. M-σ and L-σ corresponds to index errors at the resolution of the *MILES* and Lick/IDS libraries, respectively. T98-σ are the index errors presented in Trager et al. (1998) for the Lick/IDS library. I_{lib} are indices measured on the libraries (*MILES*, *ELODIE* and *STELIB*) for which offsets to the Lick/IDS library are presented. I_L are indices measured on the Lick/IDS library.

INDEX		**Error**			**Offset** $I_{lib} = a \cdot I_{Lick} + b$					
					MILES		ELODIE		STELIB	
i	NAME	M-σ	L-σ	T98-σ	a	b	a	b	a	b
1	Hδ_A	0.164	0.125	0.64	0.960	-0.054	0.955	0.721	0.940	0.823
2	Hδ_F	0.093	0.075	0.40	0.965	0.049	0.936	0.397	0.956	0.242
3	CN$_1$	0.0042	0.0038	0.018	0.912	0.008	0.897	-0.012	0.986	-0.010
4	CN$_2$	0.0050	0.0042	0.019	0.907	0.006	0.900	-0.008	0.985	-0.013
5	Ca4227	0.063	0.047	0.25	0.904	0.074	0.771	0.163	0.918	-0.057
6	G4300	0.112	0.093	0.33	0.858	0.625	0.870	0.646	0.924	0.565
7	Hγ_A	0.142	0.107	0.48	0.976	-0.148	0.967	-0.057	1.022	-0.735
8	Hγ_F	0.069	0.059	0.33	0.963	-0.038	0.962	0.016	0.999	-0.238
9	Fe4383	0.155	0.127	0.46	0.932	-0.220	0.929	-0.184	0.915	0.796
10	Ca4455	0.073	0.056	0.22	0.747	-0.067	0.785	-0.105	0.891	-0.228
11	Fe4531	0.122	0.096	0.37	0.857	0.290	0.838	0.390	0.877	-0.002
12	C$_2$4668	0.179	0.156	0.57	0.903	0.484	0.913	0.295	0.992	0.512
13	Hβ	0.063	0.051	0.19	0.981	0.126	0.996	0.015	1.004	0.032
14	Fe5015	0.139	0.115	0.41	0.902	0.084	0.926	0.178	0.989	0.168
15	Mg$_1$	0.0017	0.0013	0.006	0.911	0.0004	0.923	0.005	0.903	-0.009
16	Mg$_2$	0.0023	0.0014	0.007	0.918	-0.003	0.940	0.0006	0.960	-0.013
17	Mgb	0.053	0.045	0.20	0.964	0.108	0.935	0.247	1.003	-0.026
18	Fe5270	0.058	0.047	0.24	0.923	0.101	0.919	0.180	0.932	0.173
19	Fe5335	0.063	0.044	0.22	0.960	0.135	0.963	0.032	0.946	0.110
20	Fe5406	0.044	0.031	0.18	0.874	0.269	0.913	0.165	0.853	0.264
21	Fe5709	0.060	0.050	0.16	0.979	-0.026	0.907	0.015	1.019	-0.046
22	Fe5782	0.057	0.043	0.19	0.920	0.037	0.879	-0.004	0.906	0.088
23	Na D	0.082	0.064	0.21	0.990	-0.162	0.979	-0.069	0.993	-0.071
24	TiO$_1$	0.0021	0.0017	0.006	0.918	-0.005	0.895	-0.006	0.918	0.0003
25	TiO$_2$	0.0022	0.0016	0.006	0.904	0.0007	0.912	0.005	0.940	0.009

assigned a solar metallicity to increase the number of data points.

2.1 Empirical stellar Lick indices

Our aim was to produce fitting functions both for the resolution of the *MILES* library (2.3 Å) and for the resolution of the Lick/IDS library (8-11 Å). We have therefore measured the 25 Lick indices directly on the original stellar spectra and on the spectra downgraded to the Lick/IDS resolution described by the curve presented in Worthey & Ottaviani (1997). We have used the index definitions from Trager et al. (1998) and also from Worthey & Ottaviani (1997) for the higher order Balmer lines (Hδ_A, Hδ_F, Hγ_A and Hγ_F). Observational errors and offsets to the Lick/IDS library are described in the following paragraphs.

2.1.1 Observational index errors

We have derived typical observational index errors in order to evaluate the quality of our index measurements. To this end we have used pixel 1-σ observational errors (P. Sánchez-Blázquez private communication) to perturb each stellar spectrum, both at *MILES* resolution and Lick/IDS resolution, through 600 Monte Carlo realizations. We have then measured the 25 Lick indices for each perturbed spectrum and determined 1-σ errors for each index by using the spread in index measurements from the realizations. The index errors of the individual stellar spectra are used for weighting the least square fits when deriving both the offsets to the Lick system (Section 2.1.2) and the fitting functions (Section 3).

Trends between the index errors and the atmospheric parameters or line-strength indices can in principle bias the fits, but we have found such trends not to affect the results. Only for the Balmer indices we find weak trends of increasing errors with decreasing temperature and decreasing index strength. No trends with logg and Fe/H are found for the Balmer indices. These weak trends can probably be explained with higher S/N for bright hot stars where the Balmer indices increase significantly in strength. Since we compute the fitting functions in bins of temperature, these trends have no significant effects on the final fitting functions.

The final 1-σ typical index errors were determined by taking the median error of the whole stellar library for each index. The typical index errors are presented in Table 1 both for *MILES* and Lick/IDS resolution. Compared to the typical index errors for the Lick/IDS stellar library (Trager et al. 1998), also included in Table 1, we find the errors of the MILES library to have improved significantly. The stars of the Lick/IDS library were observed about thirty years before the *MILES* library. Considering the technical development in thirty years time, an improvement in the measured indices ought to be expected.

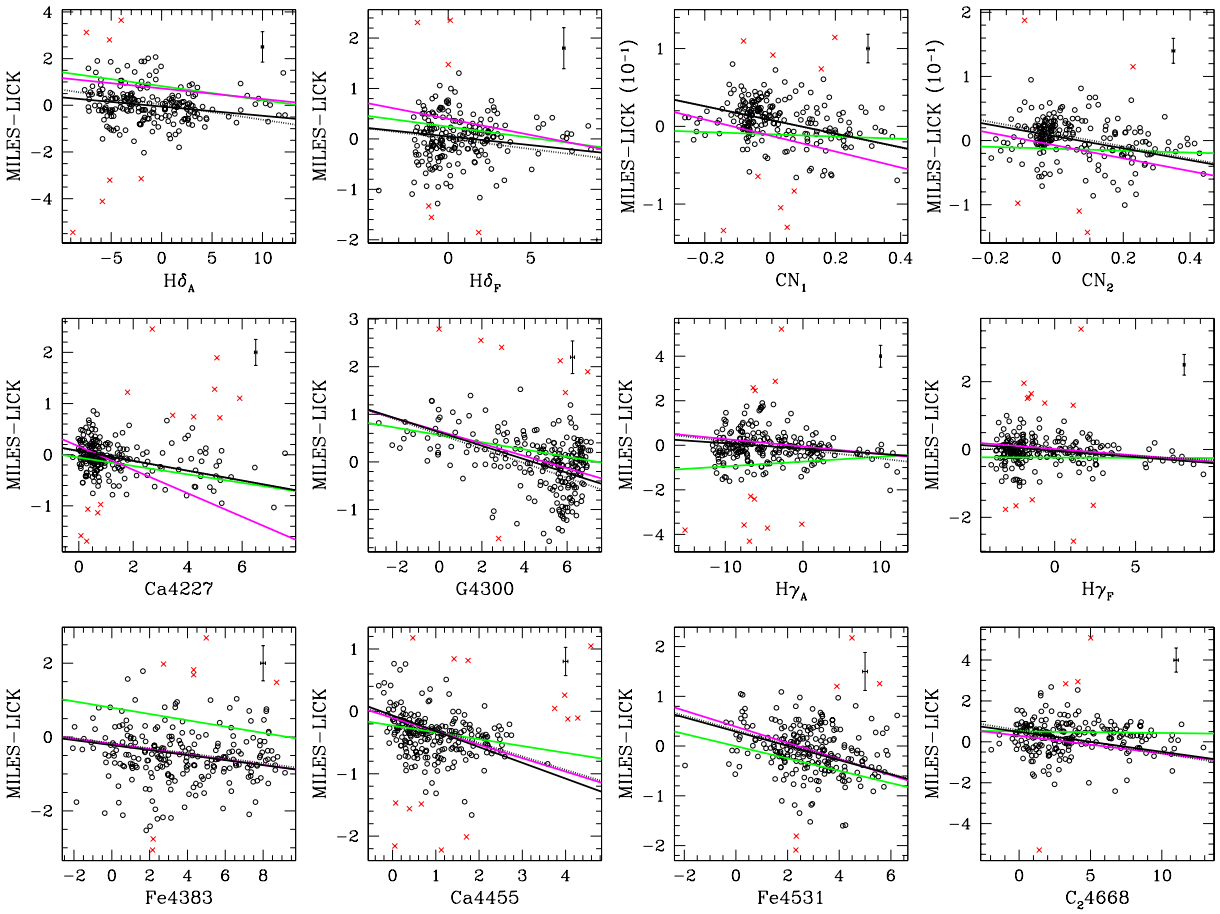

Figure 1. Index by index comparison between index strengths measured on the MILES library and the Lick/IDS library. Each panel shows the residual as a function of index strength. Included are also least-square fits of the residuals (black lines, coefficients presented in Table 1) that show clear index strength dependent offsets between the two libraries. Red crosses are sigma clipped data points in the least-square fitting routine. Typical index errors are indicated in the right top corners (see text for more details). Included are also offsets to the Lick/IDS library derived in this work for the *ELODIE* (magenta lines) and *STELIB* (green lines) libraries, as well as the offsets derived in Sánchez-Blázquez et al. (2009) for the *MILES* library (dotted lines).

2.1.2 Lick Index offsets

We have computed Lick index offsets between the *MILES* library and the Lick/IDS library using the stars in common between the two libraries. These offsets can be used for comparisons between models based on this work with models based on the Worthey et al. (1994) and Worthey & Ottaviani (1997) fitting functions. The offsets are also used in Section 4 to compare the fitting functions of this work with the fitting functions of Worthey et al. (1994) and Worthey & Ottaviani (1997).

Fig. 1 shows index by index comparisons for the residuals between the index measurements of the two libraries as function of index strength. Worthey & Ottaviani (1997), Kuntschner (2001) and Schiavon (2007) computed zero-point offsets to the Lick/IDS library, while Puzia et al. (2002) computed their offsets as 2nd order least-square fits. For most indices we find index strength dependent residuals between the two libraries (Fig. 1). We have therefore computed the offsets using a sigma-clipping linear least-square fitting routine, weighted with the individual index errors derived in Section 2.1.1. The slope and intercept of these fits are presented in Table 1 and also included in Fig. 1 (black solid lines). Sigma-clipped data points are indicated with red crosses in Fig. 1 and the error bars are the 1-σ index errors presented in Section 2.1.1. The error bars along the x-axes are represented by the index errors derived for the *MILES* library, while the error bars along the y-axes are represented by the combined errors of the *MILES* and Lick/IDS libraries in quadrature.

Extreme outliers, i.e. data points that clearly showed strong deviating values compared to the bulk of data points, were removed prior to running the fitting routine, in order to avoid stars with anomalous index strengths to affect the final fits. For three indices ($C_2$4668, Fe5015 and Mgb) we found offsets at particularly high index strengths that deviated from the offset trends for the majority of data points. The low number of data points at these index strengths and the absence of data points at intermediate index strengths induced a bias in the derived offsets. The data points at particularly high index strengths were therefore discarded when determining the final offsets.

Offsets between the *MILES* and the Lick/IDS library derived in Sánchez-Blázquez et al. (2009) are also included

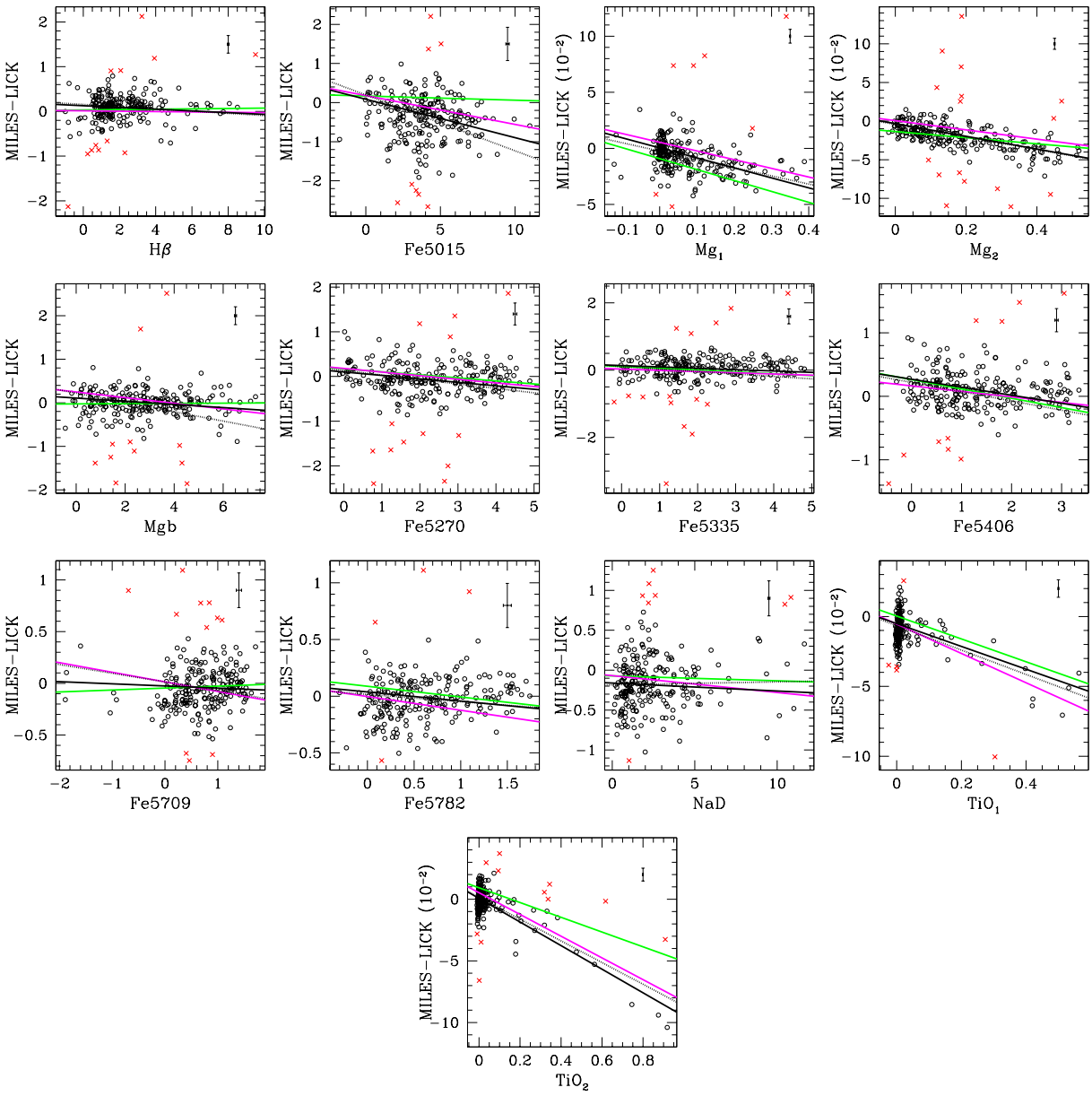

Figure 1 – *continued*

in Fig. 1 (dotted lines). These offsets and the offsets derived in this work for the *MILES* library show in general very good agreement. Differences greater than the 1-σ index errors are mainly found for Mgb, one of the indices for which we excluded data points at high index strengths due to deviations in offset trends. Noticeable offset differences, but still within the 1-σ index errors, are also found for Fe5015, Fe5709, NaD, TiO_1 and TiO_2. Only small deviations are found between the offsets derived in Sánchez-Blázquez et al. (2009) and in this work for the rest of the indices.

For comparison, and for the derivation of a possible universal offset between flux-calibrated system and the Lick/IDS system, we have also determined offsets to the Lick/IDS library for two other flux-calibrated stellar libraries, namely *ELODIE* (Prugniel & Soubiran 2001) and *STELIB* (Le Borgne et al. 2003). These offsets were determined using the same procedure as described above for the *MILES* library, except that no individual index errors were used as weights in the least-square fitting. For *STELIB* the lack of information did not allow for a computation of index errors, while the derived index errors for *ELODIE* were found to be unreliable as they showed unrealisticly small values. Since we only found small deviations in the offsets derived for the *MILES* library when not weighting as compared to weighting the least-square fits, we compare the offsets derived for all three libraries.

In accordance with the *MILES* library we found index strength dependent offsets also for the *ELODIE* and *STELIB* libraries. We found deviating offsets trends at high index values for the same indices as for the *MILES* library ($C_2$4668, Fe5015 and Mgb).

The offsets derived for the *ELODIE* and *STELIB* li-

braries are also presented in Table 1 and Fig. 1 (magenta and green lines, respectively). Clearly, deviations in the offsets are found between the libraries, especially for the *STELIB* library compared to the other two libraries. However, the *STELIB* library is also the library having the least number of stars in common with the Lick/IDS library, giving a higher statistical uncertainty in the derived offsets. The *STELIB* library only has 44 stars in common with the Lick/IDS library, while *ELODIE* has 112 stars and the *MILES* library has 237 stars in common with the Lick/IDS library. Ca4227 showed particularly strange behaviour with index strength and the accuracy of the final offsets for this index could be questionable.

In Fig. 1 we find agreements within the 1-σ index errors between the offsets derived for all three libraries for Hβ, Mgb, Fe5270, Fe5335, Fe5406, Fe5709, Fe5782 and NaD. This implies a better agreement between all libraries at wavelengths redder than $\sim$4800 Å, with the exception for the broader molecular indices Mg_1, Mg_2, TiO_1 and TiO_2 that show differences greater than the 1-σ index errors, which is also found for Fe5015. Agreements between offsets derived for *MILES* and *ELODIE* only, well within the 1-σ index errors, are found for G4300, Hγ_A, Hγ_F, Fe4383, Ca4455, Fe4531 and $C_2$4668. This instead implies a worse agreement between *MILES* and *ELODIE* at wavelengths bluer than $\sim$4250 Å (Hδ_A, Hδ_F, CN_1, CN_2 and Ca4227), where we in general find inconsistencies between all three libraries. The significant deviation in offset between the libraries for several indices hamper the derivation of a universal offset between the Lick/IDS and flux-calibrated systems as described by these libraries.

This conclusion gets further support from the study of Sánchez-Blázquez et al. (2006) who show that offsets exist between the three flux-calibrated libraries *MILES*, *STELIB* and *ELODIE*. These offsets are generally in good agreement with the individual Lick offsets found in this work.

3 FITTING FUNCTIONS

In order to produce empirical fitting functions for the MILES library, we combine our measured Lick indices with the corresponding stellar atmospheric parameters (see Section 2). It is a complex task to find the best relationship between indices and stellar atmospheric parameters, with several methods available in the literature. The method adopted in this work is presented in this section along with the derived fitting functions.

A user friendly Fortran 90 code is available online at www.icg.port.ac.uk/$\sim$johanssj to make the implementation of our fitting functions easier.

3.1 Fitting method

The relationship between Lick index strengths and stellar parameters shows a complex behaviour, making it difficult to find one reliable empirical fitting function for the whole parameter space. To solve this problem the parameter space must be divided into subregions where local fitting functions can be computed. However, it is desirable to find the simplest set of fitting functions and achieve a final representation of the data that is as accurate as possible. Hence the limits of the subregions have to be carefully chosen. It has also to be assured that adjacent subregions overlap, making smooth transitions possible. For these transitions we have adopted cosine-weighted interpolations following Cenarro et al. (2002). The choice of subregions are discussed in Section 3.2.

Following the extensive number of published fitting functions in the literature (Worthey et al. 1994; Gorgas et al. 1999; Cenarro et al. 2002; Schiavon 2007; Maraston et al. 2009), we use a linear least square fitting routine to determine the local relationships as polynomials in the following way

$$I(\theta, [Fe/H], logg) = \sum_i \beta_i \cdot \theta^j \cdot [Fe/H]^k \cdot logg^l \qquad (1)$$

where $j, k, l \geqslant 0$ and the atmospheric effective temperature is represented by $\theta = 5040/T_{\rm eff}$. The representation of $T_{\rm eff}$ using θ is chosen due to the wide range of spectral types in the stellar library. The number of terms in Eq. 1 can be made arbitrarily high. However, the goal is to find the best compromise between simplicity and accuracy by discarding terms with higher order polynomials that are negligible or induce unphysical behaviours. To this end several methods have been developed in the literature. Worthey et al. (1994) presented a method to find the converging rms scatter by successively including terms and test if the rms scatter was significantly reduced by means of a F-test. Gorgas et al. (1999) and Cenarro et al. (2002) instead test if each term significantly differed from zero through a T-test. Schiavon (2007) point out that both methods mentioned above are sensitive to the coverage of parameter space. Therefore Schiavon (2007) combine the two methods by first successively removing statistically insignificant terms and then interactively testing the remaining terms for unphysical behaviours and their effect on the rms scatter.

In this work we adopt a mix of the above mentioned methods. We choose successive inclusion over successive removal of terms. The main reason for this choice is that the normal equations of the linear least square routine run a high risk of becoming degenerate when terms that respond similarly to the data are combined. By including terms we can better control the degeneracy of the normal equations. If degenerate normal equations were reached after the inclusion of a new term, this new term was discarded since a possible lower order term already responded to the data in a similar fashion.

Finally, we determined the local fitting functions through an error weighted linear least square routine (for individual index errors see Section 2.1.1). Terms were successively included following the procedure described in Gorgas et al. (1999), by starting with the constant ($j, k, l = 0$ in Eq. 1) and then increasing the sum of powers $j+k+l$ up to a maximum of $j + k + l = 3$, including all possible cross terms. However, since the effective temperature is the parameter showing the most complex behaviour we included polynomials of θ up to $j = 5$. If the variance was not reduced at the inclusion of a new term the term was discarded. When a reduced variance was found the new term and all the previously included terms were tested by means of a T-test to determine if the coefficients β_i were statistically different from zero (by using the coefficient errors following Gorgas et al. 1999 and Cenarro et al. 2002). Terms with coefficients having a significance level $\alpha \leqslant 0.1$ was kept. We

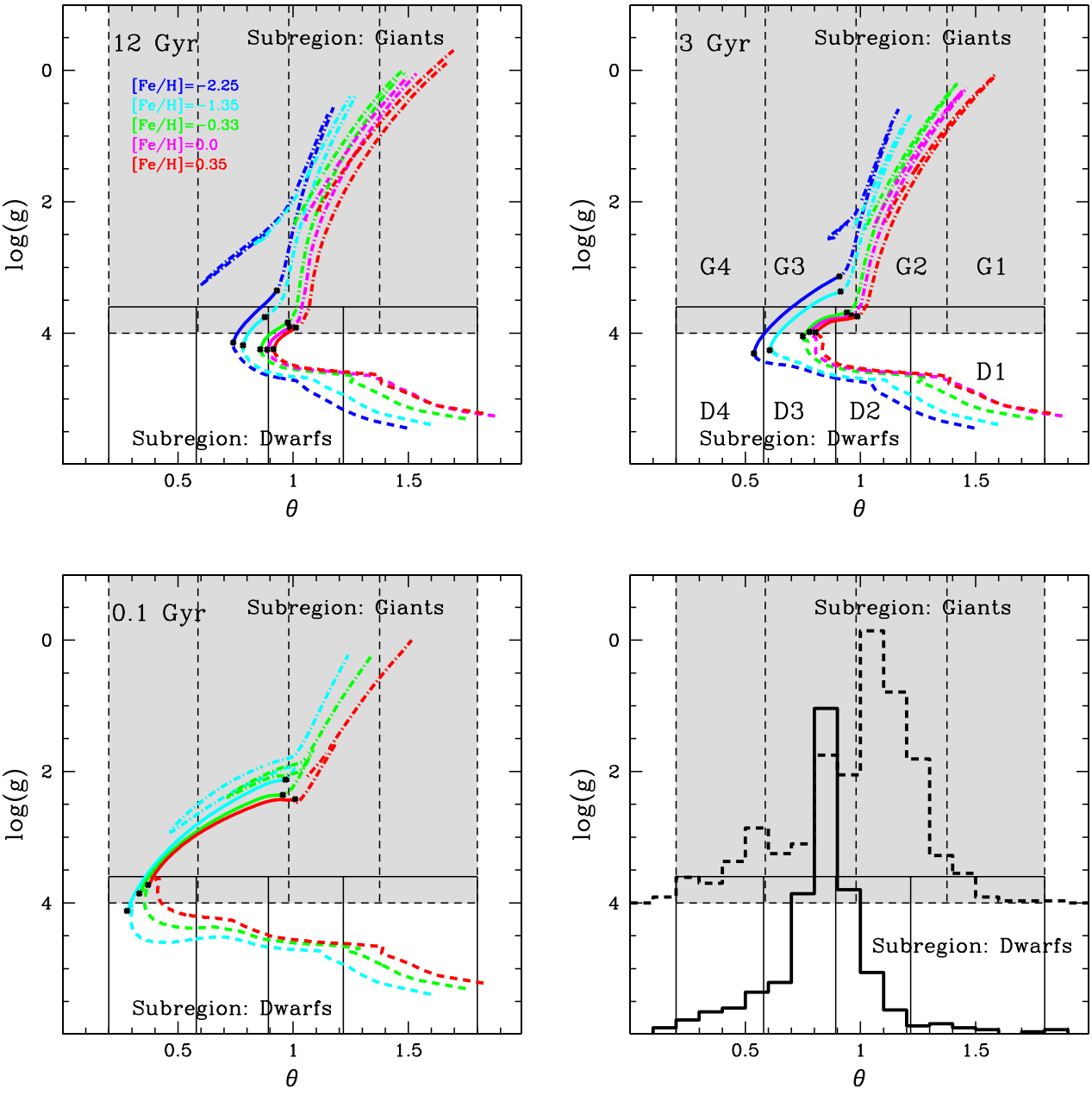

Figure 2. The top panels and the lower left panel show the relationship between the chosen subregions and the analogous in the stellar population models of Maraston (2005). The three panels show models for different ages (as indicated) and for each age the models are presented for varying metallicities as indicated by the corresponding colors. Each single model is divided into the main-sequence (dashed lines), sub-giant branch (solid line) and the rest of the post-main-sequence phases (dash-dotted lines). The lower right panel shows the relationship between the chosen subregions and the distribution of data points as a function of $\theta/T_{\rm eff}$ for *Dwarfs* ($\log g > 3.6$, solid lined histogram) and *Giants* ($\log g > 4.0$, dashed line histogram) separately. In all panels the $\theta/T_{\rm eff}$ subregions for the *Dwarf* subregion (solid lines) are indicated with D1-4 and for the *Giant* subregion (shaded area and dashed lines) with G1-4.

then interactively studied the fitting functions and removed terms inducing unphysical behaviours or not affecting the rms scatter significantly. At the end of each run the sample was σ-clipped, by removing data points deviating more than 3 σ, and the fitting redone on the new sample.

Extreme outliers that clearly deviated from the bulk of data points were discarded prior to running the fitting routine. Hence to avoid stars with anomalous index strengths affecting the fitting functions.

3.2 Definition of subregions in parameter space

Thanks to the good coverage of stellar parameters the *MILES* library show a complex behaviour of the relation-

Table 2. Fe5335 fitting function coefficients for Lick/IDS resolution

	overall rms=0.2586							
	$\log g \leqslant 4.0$ and θ limits:				$\log g \geqslant 3.6$ and θ limits:			
Term	$\leqslant 0.58$	$0.50-1.1$	$0.95-1.5$	$\geqslant 1.2$	$\leqslant 0.58$	$0.50-1.0$	$0.85-1.4$	$\geqslant 1.2$
Const.	-0.05682	-1.257	125.1	-279.0	-0.8217	-43.41	56.65	10.18
θ	0.4726	1.861	-343.3	591.9	9.547	217.8	-190.9	-4.614
[Fe/H]	x	-0.6719	x	x	x	1.336	-14.42	0.6270
$\log g$	x	x	x	x	x	x	0.3445	x
θ^2	x	1.797	314.1	-406.0	-30.62	-397.3	205.6	x
$[Fe/H]^2$	x	x	x	x	x	x	0.9821	x
θ[Fe/H]	x	1.808	1.048	x	x	-4.202	31.08	x
θ^3	x	x	-93.45	90.94	30.84	313.2	-69.81	x
$[Fe/H]^3$	x	-0.05781	-0.1268	x	x	x	x	x
θ^2[Fe/H]	x	x	x	x	x	4.535	-15.09	x
$\theta[Fe/H]^2$	x	x	-0.2159	x	x	0.2707	-0.7390	x
θ^4	x	x	x	x	x	-87.19	x	x
rms	0.1111	0.2352	0.3446	0.7921	0.08168	0.1348	0.1879	0.7221
N	81	358	365	113	51	349	207	17

Table 3. Fe5335 fitting function coefficient errors for Lick/IDS resolution

	$\log g \leqslant 4.0$ and θ limits:				$\log g \geqslant 3.6$ and θ limits:			
Term	$\leqslant 0.58$	$0.50-1.1$	$0.95-1.5$	$\geqslant 1.2$	$\leqslant 0.58$	$0.50-1.0$	$0.85-1.4$	$\geqslant 1.2$
Const.	0.01305	0.04702	1.237	2.860	0.1784	2.914	2.000	0.06966
θ	0.03082	0.1169	3.120	5.928	1.544	15.82	5.800	0.04788
[Fe/H]	x	0.01732	x	x	x	0.1617	0.3727	0.01636
$\log g$	x	x	x	x	x	x	0.01056	x
θ^2	x	0.07110	2.603	4.059	4.200	31.77	5.571	x
$[Fe/H]^2$	x	x	x	x	x	x	0.08236	x
θ[Fe/H]	x	0.01959	0.008170	x	x	0.4293	0.7186	x
θ^3	x	x	0.7181	x	3.624	27.99	1.772	x
$[Fe/H]^3$	x	0.001251	0.003640	x	x	x	x	x
θ^2[Fe/H]	x	x	x	x	x	0.2782	0.3495	x
$\theta[Fe/H]^2$	x	x	0.01012	x	x	0.005307	0.08761	x
θ^4	x	x	x	x	x	9.138	x	x

ship between the Lick indices and the stellar parameters. We have therefore divided parameter space into several subregions.

The relationship between the Lick indices and the stellar parameters show a bimodality between high and low gravity stars (i.e. *Giants* and *Dwarfs*). The first major subregions that we have chosen are therefore in high and low values of $\log g$ space (from now on referred to as the *Dwarf* and *Giant* subregion, respectively), in accordance with Gorgas et al. (1999), Cenarro et al. (2002) and Schiavon (2007). The same $\log g$ subregion limits have been used for all indices. The lower limit for the *Dwarf* subregion was set to $\log g = 3.6$, while the upper limit for the *Giant* subregion was set to $\log g = 4.0$, giving an overlap region of $\Delta \log g = 0.4$. In Fig 2 the subregions are shown together with the analogous in the stellar population models of Maraston (2005), for $\log g$ as a function of θ. The different evolutionary phases for the models are indicated in Fig 2. This shows that the choice of limits for the *Dwarf* and *Giant* subregions coincides very well with the division into the main-sequence and the post-main-sequence, as the $\log g$ overlap region mainly covers the sub-giant branch (SGB).

To fully recover the detailed behaviour within the $\log g$ subregions we divided the full $\theta/T_{\rm eff}$ range into four subregions. The choice of the limits for $\theta/T_{\rm eff}$ subregions follow the behaviour of the models and the distribution of stars as a function $\theta/T_{\rm eff}$. This can be seen in Fig 2 where the limits of the $\theta/T_{\rm eff}$ subregions are represented by the midpoints in the overlap regions, averaged over all indices. The $\theta/T_{\rm eff}$ subregions are discussed in the following bullet points, by referring to the $\theta/T_{\rm eff}$ subregions using the names (D1-4 and G1-4) in Fig 2, first for the *Giant* subregion

- Only the tip of the RGB for high metallicities fall within G1 (Fig 2). The lower limit (in θ) for this subregion coincides with the strong drop-off in the distribution of data points (Fig 2). With the weak dependency on metallicity for this subregion and the low number of data points we fit this subregion independently of metallicity.
- G2 and G3 clearly separates out the red-giant branch (RGB) to be fitted mainly in G2 (Fig 2).
- Most indices show a distinct change in the behaviour of the index strengths as a function of the stellar parameters for hot A-type stars, around $\theta = 0.5-0.6$, see Fig. 3 and Fig. A1-A24. The overlap regions between G3 and G4 are therefore located around this range in θ.

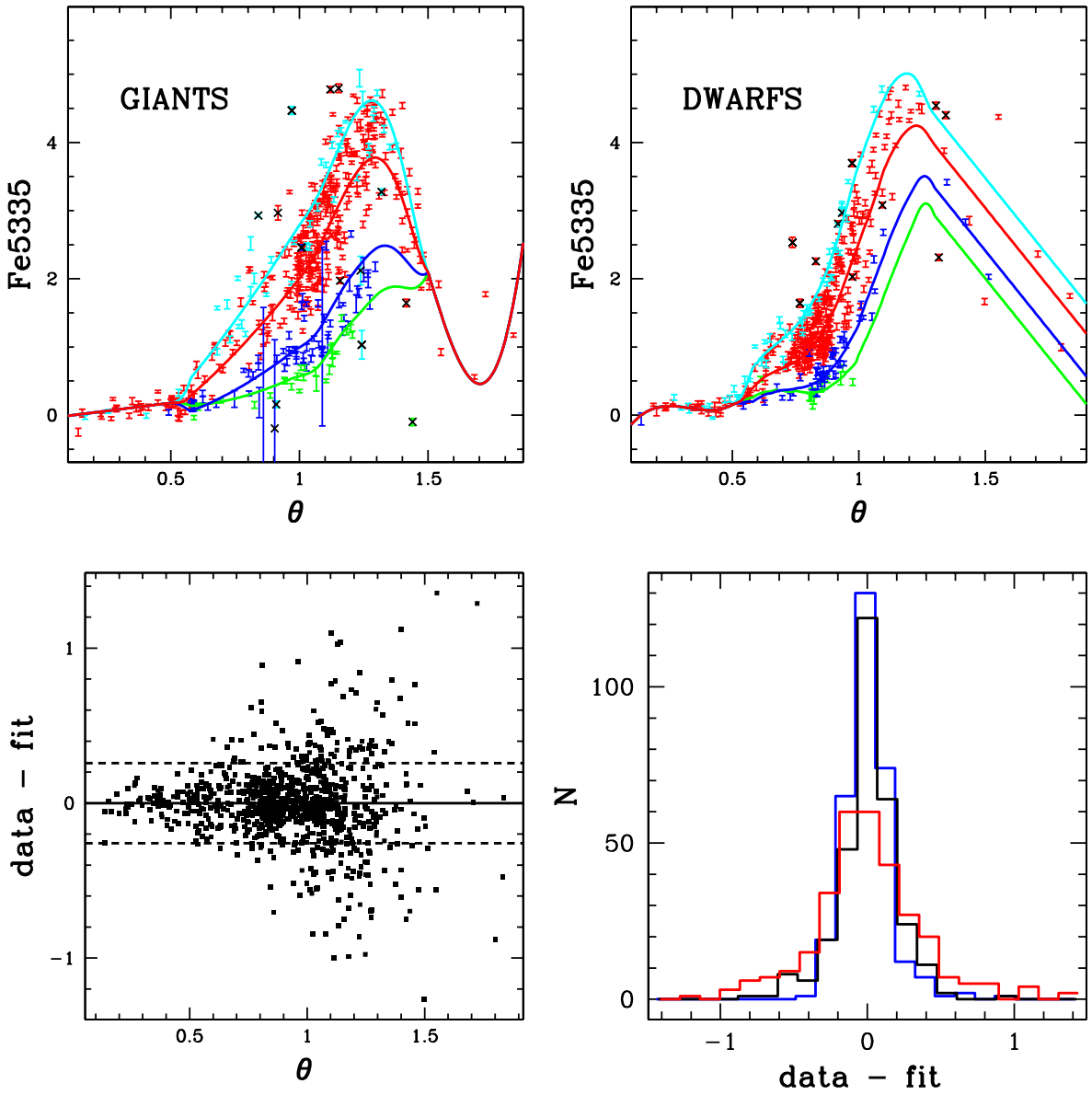

Figure 3. The fitting functions for Fe5335 (Lick resolution) are shown in the upper panels for various metallicities and over-plotted on data in corresponding metallicity bins. The error bars on the data are observational index errors (see Section 2.1.1). The colors correspond to [Fe/H]= −2.0 (green) , [Fe/H]= −1.35 (blue), [Fe/H]= −0.35 (red) and [Fe/H]= 0.35 (cyan) for the fitting functions and [Fe/H]< −1.8 (green) , −1.8 <[Fe/H]< −1.0 (blue), −1.0 <[Fe/H]< 0.2 (red) and [Fe/H]> 0.2 (cyan) for the data. The left and right upper panels show Giants ($\log g < 3.6$) and Dwarfs ($\log g > 3.6$) , respectively, for the average $\log g$ of the data in bins of $\Delta\theta = 0.1$ at steps of $\theta = 0.01$. Fixed $\log g$ values are used at the ends of the $\theta/T_{\rm eff}$ range, with $\log g = 1.0, 2.0$ (cold,warm end) and $\log g = 4.6, 4.0$ (cold,warm end) for Giants and Dwarfs, respectively. Data points with black crosses have been sigma clipped by the least-square fitting routine. The lower left panel shows the residuals between the data and the fitting functions as a function of θ and the dashed lines represents the overall rms value for the fitting functions. The lower right panel shows the distribution of the residuals for three $\theta/T_{\rm eff}$ bins, indicated by different colors where blue have $\theta < 0.841$ black $0.841 \geqslant \theta < 1.045$ and red $\theta \geqslant 1.045$.

and then for the *Dwarf* subregion

- The lowest part of the main-sequence fall within D1 (Fig. 2). As for the *Giant* subregion, the lower limit (in θ) for this subregion coincides with the strong drop-off in the distribution of data points.
- The division of $\theta/T_{\rm eff}$ space into D2 and D3 were found to improve the fits in terms of a significantly reduced rms scatter.
- As for the *Giant* subregion, most indices show a distinct change in the behaviour of the index strengths as a function of the stellar parameters for hot A-type stars, around $\theta = 0.5 - 0.6$, see Fig. 3 and Fig. A1-A24. The overlap regions between D3 and D4 are therefore located around this range in θ.

The number of the $\theta/T_{\rm eff}$ subregions is the same for all indices. With the exceptions for TiO_1 and TiO_2 that

show a much simpler behaviour and we have therefore used less $\theta/T_{\rm eff}$ subregions (see Fig. A23-A24, Table A23-A24 and Table B24-B25). Since the different indices show a varying dependence on the stellar parameters, the limits for the subregions have been adjusted for each index individually to reduce the rms scatter.

The choice of subregions in $\log g$ and $\theta/\mathrm{T_{eff}}$ space make up the base for our fitting functions. On top of these, metallicity space had to be divided into two subregions for 10 indices ($\mathrm{CN_1}$, $\mathrm{CN_2}$, Ca4227, G4300, Fe4383, Fe5015, $\mathrm{Mg_1}$, $\mathrm{Mg_2}$, Mgb and NaD) in order to fully reproduce the metal-poor end, but only in the low gravity subregion and in the specific temperature range around $1.0 < \theta < 1.4$ ($5040 < T_{\rm eff} < 3600$). We have therefore independently fitted metal-rich and metal-poor stars, divided at [Fe/H]~ -1.0 for the affected temperatures in the low gravity subregion for the 12 indices.

Even though the *MILES* library covers an extensive range of stellar parameter space, the very ends are obviously still sparsely populated. Therefore, the fitting functions are not valid beyond $\theta > 1.8$ ($T_{\rm eff} < 2800$) and $\theta < 0.2$ ($T_{\rm eff} > 25200$). The dwarf main-sequence that extends to very low temperatures is well covered within these limits (Fig. 2). Very hot young stars with temperatures greater than 25200 K do not have strong indices in the visual parts of their spectra.

3.3 [α/Fe] trends

Globular cluster stars are significantly [α/Fe]-enhanced with respect to solar values (~ 0.3, Carney 1996). The [α/Fe]-trend of field stars in the solar neighborhood instead show increasing [α/Fe]-enhancements with decreasing metallicity down to [Fe/H]~ -1.0 (Edvardsson et al. 1993; Fuhrmann 1998; Milone, Sansom & Sánchez-Blázquez 2009). It is first at this metallicity that the field stars reach globular cluster [α/Fe]-values. Having globular cluster stars for [Fe/H]> -1.0 can therefore induce [α/Fe] trends biased towards globular cluster values in stellar libraries dominated by field stars. The globular cluster M71 has a metallicity of [Fe/H]$= -0.84$ and is represented by a significant number of 28 stars in the *MILES* library, which could possibly induce such a bias. The stars from this globular cluster were therefore discarded when computing the final fitting functions, since the *MILES* library is reasonably well populated with field stars around the metallicity of M71.

The [α/Fe]-bias of the solar neighborhood must be taken into account when deriving stellar population models based on empirical stellar libraries, as discussed in Maraston et al. (2003). Model adjustments are therefore needed when adopting the fitting functions of this work. Such adjustments are described in Tripicco & Bell (1995); Thomas et al. (2003, 2004); Korn et al. (2005); Thomas et al. (2005).

3.4 Spectral resolution

We have computed fitting functions for both the *MILES* and Lick/IDS resolutions (see Section 2.1). The same final set of terms were used for both resolutions. Coefficients and coefficient errors for the fitting functions are presented in Appendix A for Lick resolution and Appendix B for *MILES* resolution. The sigma clipped number of data points (N) for the local fitting functions are also included in the coefficient Tables, along with the rms of the residuals between the data and the final fitting functions, both local and overall. The visual behaviours, residuals and distribution of residuals of the fitting functions are shown for Lick resolution in Appendix A. An example is presented for Fe5335 and Lick resolution in Table 2 and Table 3 for coefficients and coefficient errors, respectively. The visual behaviours of the fitting functions for Fe5335 are shown in Fig. 3, where they are presented for the *Dwarf* and *Giant* subregions separately and for varying metallicity. In Appendix A the visual behaviour of fitting functions for several $\log g$ values at fixed θ are also presented for indices showing strong $\log g$ dependencies within the $\log g$ subregions.

3.5 Errors

In this section we briefly discuss possible error sources affecting the final fitting functions. Such error sources include the index measurements of the *MILES* spectra, but these show very high quality, in terms of typical observational index errors, as discussed in Section 2.1.1. However, the overall rms of the final fitting functions (see Section 3.4) are considerably larger than the typical observational index errors (see Section 2.1.1). Possible error sources for this scatter are instead uncertainties in the stellar parameter estimates and intrinsic scatter in the index strengths.

The residuals between the final fitting functions and the data, presented in the lower left panels of Fig. 3 and Fig. A1-A24 as a function of θ, show typically larger scatter for cooler temperatures where index values exhibit strong sensitivities to $\mathrm{T_{eff}}$. The source of this correlation is probably, at least partly, uncertainties in the stellar parameters, since these will have a larger effect when the index strengths show strong dependencies on the stellar parameters, i.e. $\theta/T_{\rm eff}$ uncertainties will have less effect when the index strengths show weaker dependencies on $\theta/T_{\rm eff}$.

4 COMPARISONS WITH THE LITERATURE

In this section we compare the fitting functions derived in this work with fitting functions in the literature derived for stellar libraries other than *MILES*. We search for differences in various parameter regimes. Comparisons are made with the classical and extensively adopted fitting functions of Worthey et al. (1994) and Worthey & Ottaviani (1997) (from now on WFF), shifted with the offsets derived in Section 2.1.2, and with the more recent fitting functions of Schiavon (2007) (from now on SFF) which were based on the *JONES* library (Jones 1999).

We have performed the comparisons in different regions of parameter space to find the regimes where major differences roam. The comparisons have been divided into three $\theta/T_{\rm eff}$ bins, referred to as *Cold*, *Intermediate* and *Warm* temperatures, with $\theta/T_{\rm eff}$ limits presented in Table 4. Each of these bins have been further divided into two $\log g$ bins with $\log g = 2.0$ (referred to as *Giants*) and $\log g = 4.5$ (referred to as *Dwarfs*) to make up a total of six bins. The average residuals between the fitting functions were computed in

Table 4. Limits for the different bins of $\theta/T_{\rm eff}$ space used in the fitting function comparisons. SFF-G and SFF-D correspond to the fitting functions of Schiavon (2007) for *Giants* and *Dwarfs*, respectively.

FF	***COLD*** **($T_{\rm eff}$)**	***INTER.*** **($T_{\rm eff}$)**	***WARM*** **($T_{\rm eff}$)**
WFF	2800-4582	4582-7200	7200-12263
SFF-G	2800-4582	4582-(∼)6300	-
SFF-D	3220-4582	4582-7200	7200-18000

each bin at [Fe/H] steps of 0.5 in the range $-2 \leqslant$[Fe/H]$\leqslant 0.5$ and presented in Fig. 4 and Fig. 5 as a function of metallicity for the comparisons with WFF and SFF, respectively.

The comparisons have only been made within the parameter limits for which the fitting functions are applicable, described in Worthey et al. (1994) (WFF), Schiavon (2007) (SFF) and Section 3.2 (this work), resulting in the limits of the $\theta/T_{\rm eff}$ bins presented in Table 4. Due to the limitations of the SFF we can not make comparisons for the *Warm Giant* regime, while the *Intermediate Giant* regime have a varying lower θ limit (see Schiavon 2007 for individual index limits).

The overall rms of the final fitting functions (see Section 3.4) are shown in Fig. 4 - 5 as grey shaded areas (1rms dark grey and 2rms light grey). This gives a reference to the differences found between the libraries.

Overall there is good agreement between fitting functions within the rms. We find the biggest residuals to occur at the ends of parameter space, i.e. at the metallicity and temperature ends (see Fig. 4 - 5). This was expected since the number of data points decrease towards the ends of parameter space, resulting in larger uncertainties of the fitting functions. In the rest of this Section we discuss the comparisons for individual indices in terms of stellar parameter regions that show differences beyond the 1rms and 2rms levels.

H$\delta_{\rm A}$

WFF comparison (Fig. 4): Warm Giants extend well beyond the 2rms level where this work show much weaker indices. We find both *Warm* and *Cold Dwarfs* to show stronger indices for this work, even extending beyond the 2rms level for the metal-poor and metal-rich ends, respectively. Otherwise, this work show slightly weaker indices extending to the 1rms level.
SFF comparison (Fig. 5): Cold Dwarfs show weaker indices for this work, beyond the 1rms level. *Warm* and *Intermediate* temperature *Dwarfs* show stronger indices for this work out to the 2rms level in the metal-poor regime. *Intermediate* temperature *Giants* show stronger indices out to the 2rms level at the ends of the metallicity scale. Otherwise are mainly differences within the 1rms level found.

H$\delta_{\rm F}$

WFF comparison (Fig. 4): The most obvious difference is found for *Warm Giants* where this work show much weaker indices, extending well beyond the 2rms level. Otherwise are differences mainly within the 1rms level, except for the metal-rich end of *Cold* and *Warm Dwarfs* that show stronger indices for this work beyond the 2rms level.
SFF comparison (Fig. 5): This work shows in general stronger indices in the metal-poor regime, beyond the 1 rms level for *Intermediate* temperature and *Warm Dwarfs* and beyond the 2rms level for *Intermediate* temperature *Giants*. In the metal-rich regime we instead find weaker for this work, out to the 2rms level for *Intermediate* temperature and *Cold Giants*.

CN$_1$

WFF comparison (Fig. 4): The *Warm* end for *Giants* show significantly stronger indices for this work, extending well beyond the 2rms level. Otherwise, this work show in general stronger indices at the metal-poor end and weaker indices at the metal-rich end, out to the 2rms level in both cases.
SFF comparison (Fig. 5): Intermediate temperature *Giants* and *Dwarfs* show weaker and stronger indices for this work, respectively, at the metal-rich end. Otherwise are agreements within the 1rms level mainly found.

CN$_2$

WFF comparison (Fig. 4): Similar to the previous index, but *Warm Dwarfs* show weaker indices for the entire metallicity scale for this work, out to the 2rms level.
SFF comparison (Fig. 5): Due to problems with implementing the SFFs we can not make a reliable comparison.

Ca4227

WFF comparison (Fig. 4): Cold Dwarfs show stronger indices for this work, extending out to the 2rms level in the metal-poor regime, while *Cold Giants* instead show weaker indices for this work out to the 2rms level at the metal-poor end. *Warm Giants* show stronger indices for this work beyond the 1rms level at the metal-poor end. *Cold Dwarfs* show stronger indices for this work, even extending beyond the 2rms level at the metal-poor end.
SFF comparison (Fig. 5): The most prominent difference is found for *Cold Giants* in the metal-poor regime, extending well beyond the 2rms level. *Cold Dwarfs* show stronger indices for this work at the metal-rich end, beyond the 1rms level. Otherwise are differences within the 1rms level found.

G4300

WFF comparison (Fig. 4): Warm Giants extend well beyond the 2rms level with stronger indices for this work. Metal-poor *Cold Giants* show stronger indices for this work, extending to the 2rms level. *Cold* metal-poor *Dwarfs* extend beyond the 1rms level, showing weaker indices for this work. *Cold* and *Warm* metal-rich *Dwarfs* show stronger and weaker indices for this work, respectively, beyond the 1rms level.
SFF comparison (Fig. 5): Differences beyond the 1rms and 2rms levels are found in several regimes, strongest at the ends of the metallicity scale.

H$\gamma_{\rm A}$

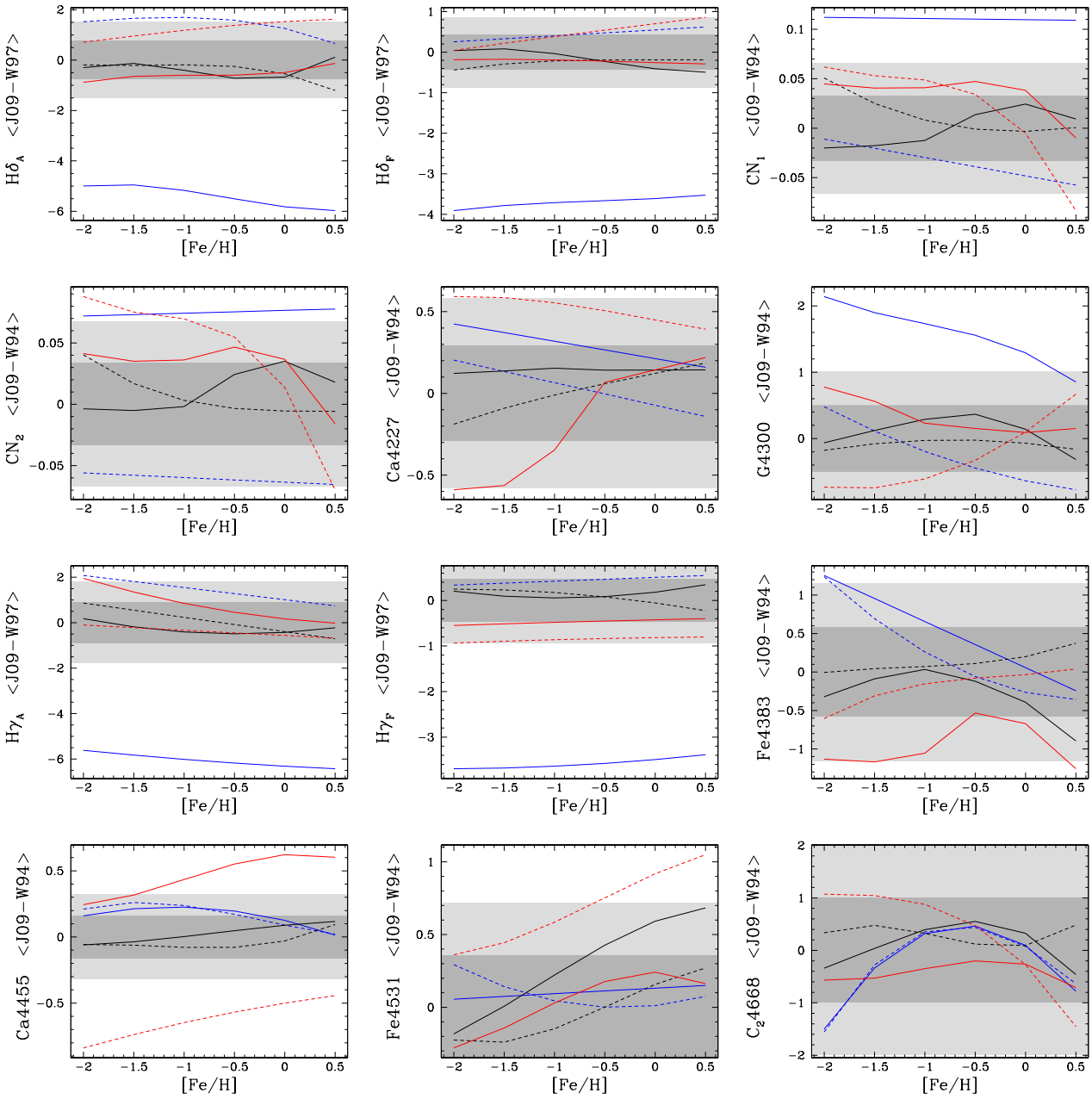

Figure 4. Comparisons between the fitting functions of this work (referred to as J09) and Worthey et al. (1994) (W94), and with Worthey & Ottaviani (1997) (W97) for $H\delta_A$, $H\delta_F$, $H\gamma_A$ and $H\gamma_F$. The panels show the difference J09-W94/W97 as a function of metallicity for each Lick index. The comparisons are made for *Giants* ($\log g = 2.0$, solid lines) and *Dwarfs* ($\log g = 4.5$, dashed lines). The different colors correspond to the different bins of $\theta/T_{\rm eff}$ space, with limits stated in Table 4, where the average difference has been computed, blue for the *Warm*, black for the *Intermediate* and red for the *Cold* temperature bin. Fitting function residuals in terms of 1rms (dark grey shaded areas) and 2rms levels (light grey shaded areas) are indicated. The errors are represented by the combined errors of the *MILES* and Lick/IDS libraries in quadrature (for more on the errors see Section 2.1.1).

WFF comparison (Fig. 4): Warm Giants show significantly weaker indices for this work, well beyond the 2rms level. *Warm Dwarfs* and *Cold Giants* show stronger indices for this work out to the 2rms level. Otherwise are mainly differences within the 1rms level found.
SFF comparison (Fig. 5): The most significant difference is found for *Intermediate* temperature *Dwarfs*, showing weaker indices for this work in the metal-poor regime well beyond the 2rms level. Otherwise are differences mainly found around the 1rms level.

$\mathbf{H\gamma_F}$

WFF comparison (Fig. 4): Weaker indices are found for this work for *Warm Giants* and *Cold Dwarfs* beyond the 2rms and 1rms level, respectively. Otherwise are mainly differences within the 1rms level found.
SFF comparison (Fig. 5): Due to problems with imple-

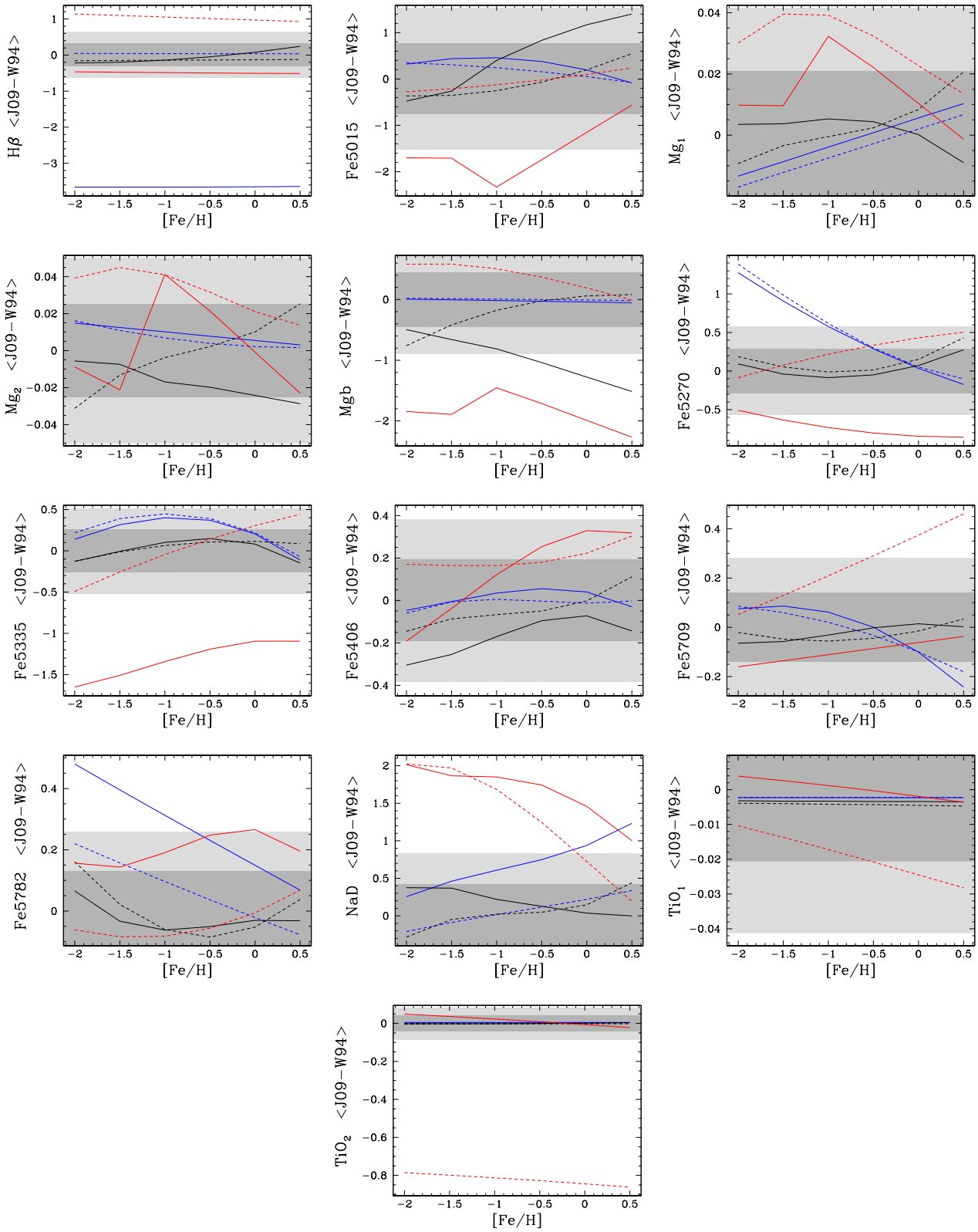

Figure 4 – *continued*

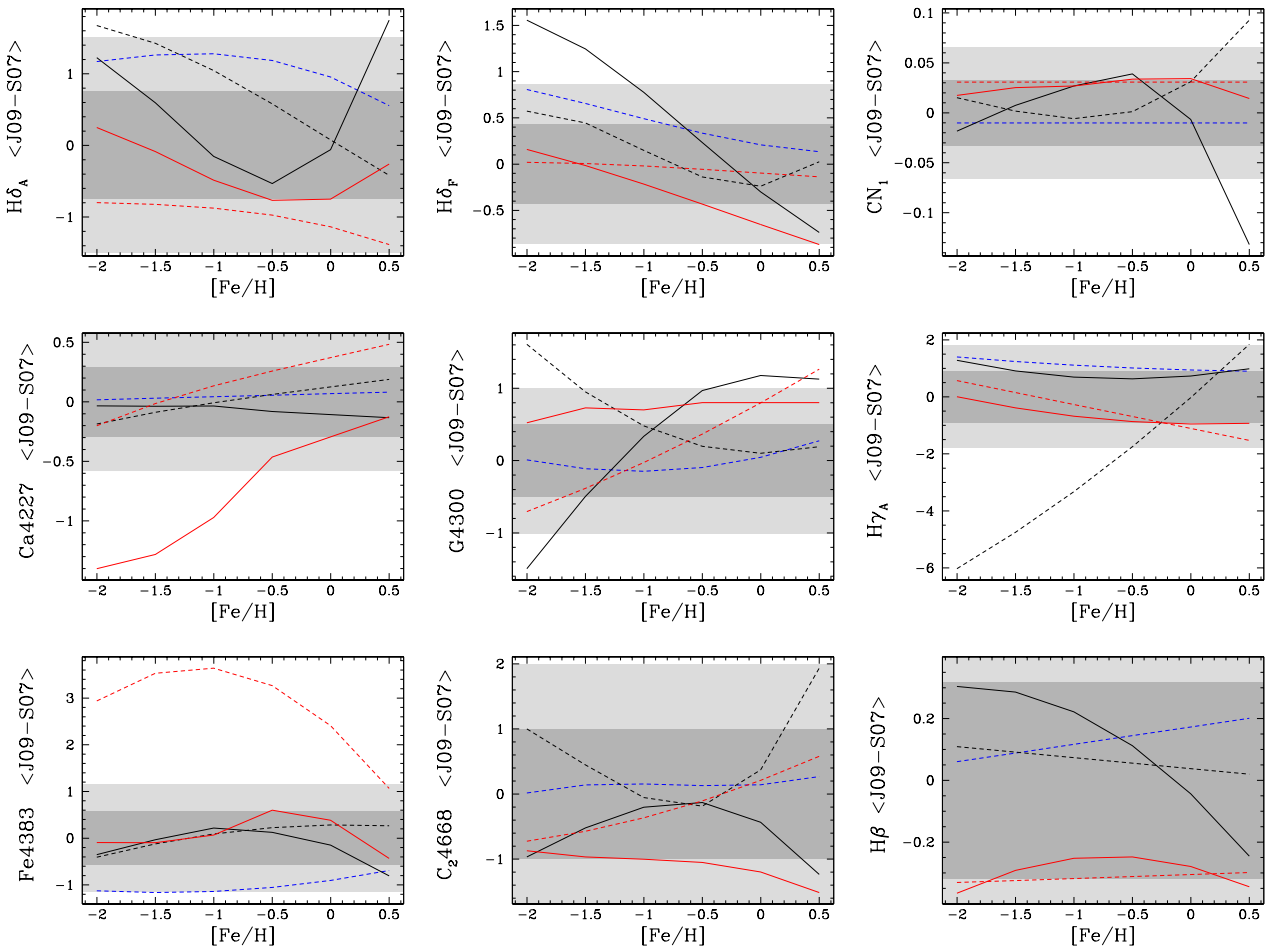

Figure 5. Same as Fig. 4, but for the comparison between this work (J09) and Schiavon (2007) (S07). The errors are represented by index errors of the *MILES* library (see Section 2.1.1).

menting the SFFs we can not make a reliable comparison.

Fe4383

WFF comparison (Fig. 4): Warm Giants and *Warm Dwarfs* show stronger indices out to the 2rms level at the metal-poor end. *Cold Giants* show weaker indices, out to the 2rms level at the metal-poor and metal-rich ends. Otherwise are mainly differences within the 1rms level found.
SFF comparison (Fig. 5): Cold Dwarfs show significantly stronger indices for this work, well beyond the 2rms level. *Warm Dwarfs* instead show weaker indices, out to the 2rms level. Otherwise are mainly differences within the 1rms found.

Ca4455

WFF comparison (Fig. 4): Cold Giants show stronger indices for this work, extending well beyond the 2rms level in the metal-rich regime. *Cold Dwarfs* show weaker indices for this work, extending well beyond the 2rms level. The *Warm* regime show stronger indices for this work, extending beyond the 1rms level in the metal-poor regime.

Fe4531

WFF comparison (Fig. 4): Cold Dwarfs show stronger indices for this work at the 1rms level for the metal-poor end and increasing well beyond the 2rms level at the metal-rich end. *Intermediate* temperature *Giants* show stronger indices for this work, out to the 2rms level at the metal-rich end.

$C_2$4668

WFF comparison (Fig. 4): The metal-rich end show weaker indices for this work, mainly down to the 1rms level. The metal-poor end show weaker and stronger indices for this work extending beyond the 1rms level for the *Warm* bins and *Cold Dwarfs*, respectively.
SFF comparison (Fig. 5): Cold Giants show weaker indices for this work beyond the 1rms level in the metal-rich regime. *Intermediate* temperature *Dwarfs* show stronger indices for this work at the metal-rich end out to the 2rms level.

Hβ

WFF comparison (Fig. 4): We find this work to show

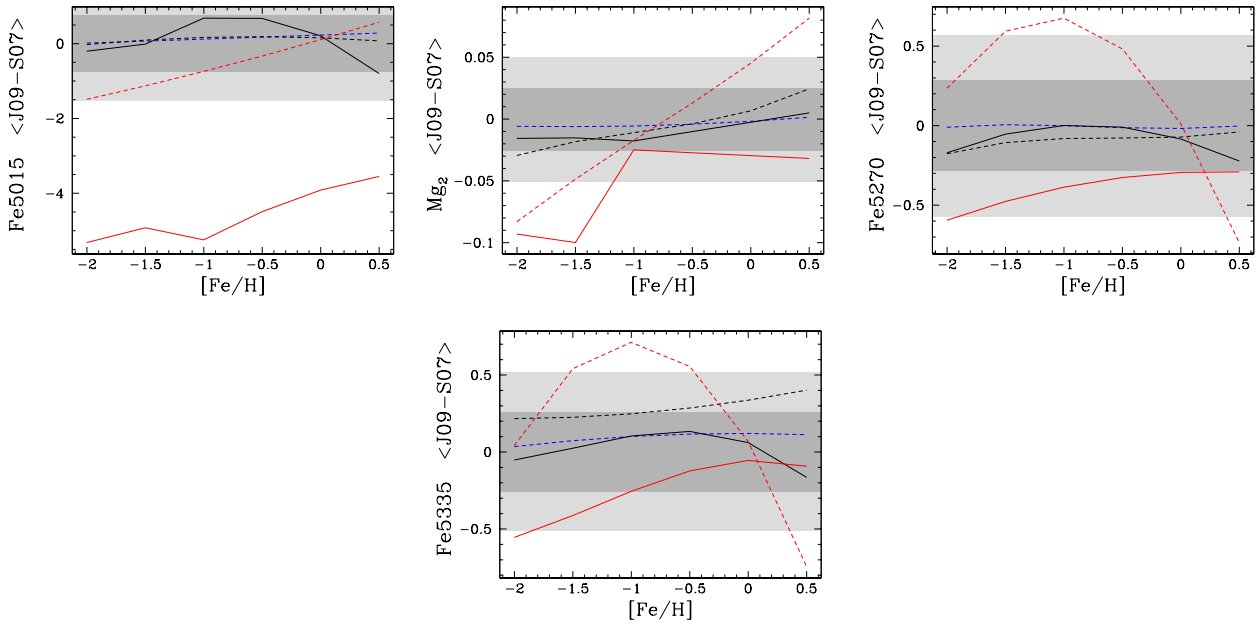

Figure 5 – *continued*

weaker indices for *Warm Giants* well beyond the 2rms level. *Cold Dwarfs* show stronger indices for this work beyond the 2rms level. *Cold Giants* show weaker indices for this work beyond the 1rms level.
SFF comparison (Fig. 5): Cold Dwarfs show the biggest differences right beyond the 1 rms level. Otherwise are differences within the 1rms level are found.

Fe5015

WFF comparison (Fig. 4): Cold Giants show weaker indices for this work, beyond the 2rms level in the metal-poor regime. *Intermediate* temperature *Giants* show stronger indices for this work beyond the 2rms level in the metal-rich regime.
SFF comparison (Fig. 5): Cold Giants show significantly weaker indices for this work, well beyond the 2rms level. This work shows weaker indices for *Cold Dwarfs* beyond the 1rms level in the metal-poor regime. Otherwise are differences within the 1rms mainly found.

Mg_1

WFF comparison (Fig. 4): The *Cold Dwarfs* show stronger indices for this work, out to the 2rms level in the metal-poor regime. The *Cold Giants* show stronger indices for this work at intermediate metallicities. No differences found beyond the 2rms level.

Mg_2

WFF comparison (Fig. 4): Cold Dwarfs show stronger indices for this work beyond the 1rms level in the metal-poor regime. *Cold Giants* show stronger indices for this work beyond the 1rms level for intermediate metallicities. Otherwise are mainly differences within the 1rms level found.

SFF comparison (Fig. 5): The *Cold* end show weaker indices for this work in the metal-poor regime, beyond the 2rms level. *Cold Dwarfs* instead show stronger indices for this work beyond the 2rms level at the metal-rich end.

Mgb

WFF comparison (Fig. 4): Cold and *Intermediate* temperature *Giants* show weaker indices for this work, extending beyond the 2rms level. *Intermediate* temperature and *Cold Dwarfs* show weaker and stronger indices, respectively, for this work in the Metal-poor regime, beyond the 1rms level.
SFF comparison (Fig. 5): Due to problems implementing the SFFs we can not make a reliable comparison.

Fe5270

WFF comparison (Fig. 4): The *Warm* end show stronger indices beyond the 2rms level in the metal-poor regime. *Cold Giants* show weaker indices for this work beyond the 2rms level. The metal-rich end show stronger indices for this work beyond the 1rms level for *intermediate* temperature *cold Dwarfs*.
SFF comparison (Fig. 5): We find weaker indices for this work beyond the 1rms level for *Cold Giants*. Stronger indices for this work beyond the 2rms level are found for *Cold Dwarfs* in the intermediate metallicity regime. Otherwise are differences well within the 1rms level found.

Fe5335

WFF comparison (Fig. 4): Cold Giants show weaker indices for this work well beyond the 2rms level. The *Warm* end show stronger indices out to the 1rms level at intermediate metallicities. *Cold Dwarfs* show weaker and stronger indices out to the 1rms level a the metal-poor and metal-rich ends, respectively.

SFF comparison (Fig. 5): Cold Dwarfs show stronger indices beyond the 2rms level at intermediate metallicities and weaker indices beyond the 2rms level at the metal-rich end. *Cold Giants* show weaker indices for this work beyond the 1rms level. *Intermediate* temperature *Dwarfs* instead show stronger indices for this work, beyond the 1rms level in the metal-rich regime.

Fe5406

WFF comparison (Fig. 4): The *Cold* end show stronger indices for this work beyond the 1rms level in the metal-rich regime. *Intermediate* temperature *Giants* show weaker indices for this work beyond the 1rms level. No differences found beyond the 2rms level.

Fe5709

WFF comparison (Fig. 4): Cold Dwarfs show stronger indices for this work, extending beyond the 2rms level at the metal-rich end. Otherwise, no significant differences beyond the 1rms level.

Fe5782

WFF comparison (Fig. 4): Warm Giants show stronger indices for this work in the metal-poor regime, extending beyond the 2rms level at the metal-poor end. *Cold Giants* show stronger indices for this work regime, beyond the 1rms level. *Warm Dwarfs* show stronger indices for this work beyond the 1rms level at the metal-poor end.

NaD

WFF comparison (Fig. 4): The *Cold* end show stronger indices for this work extending well beyond the 2rms level, especially in the metal-poor regime. *Intermediate* temperature *Giants* show stronger indices for this work, extending beyond the 2rms level in the metal-rich regime.

TiO_1

WFF comparison (Fig. 4): Cold Dwarfs show weaker indices for this work, extending well beyond the 1rms level at the metal-rich end. Otherwise, no differences found beyond the 1rms level.

TiO_2

WFF comparison (Fig. 4): We find significantly weaker indices for this work for *Cold Dwarfs*, extending very far beyond the 2rms level. Otherwise, no significant differences found beyond the 1rms level.

5 SUMMARY

We have derived new empirical fitting functions for the relationship between Lick absorption indices and stellar atmospheric parameters ($T_{\rm eff}$, [Fe/H] and $\log g$) described by the *MILES* library of stellar spectra, both for the resolution of the *MILES* library and for the resolution of the Lick/IDS library. The *MILES* library consists of 985 stars selected to produce a sample with extensive stellar parameter coverage. The *MILES* library was also chosen because it has been carefully flux-calibrated, making standard star derived offsets unnecessary. This becomes important when comparing stellar population models to high redshift data where no resolved individual stars are available.

We find the index measurements of the *MILES* spectra to have very high quality in terms of observational index errors. These errors are also found to be significantly smaller than for the Lick/IDS library. This was expected since the *MILES* library was observed nearly thirty years after the Lick/IDS library. Given the high quality of the index measurements, index errors should not be the major error sources for the final fitting functions. We instead find indications that the stellar parameter estimates are significant error sources.

Lick Index offsets between the *MILES* library and the classic Lick/IDS library are derived in order to be able to compare stellar population models based on this work with models in the literature. We find these offsets to be dependent on index strength and have therefore derived least-square fits for the residual between the two libraries. Offset to the Lick/IDS library are also derived for the flux-calibrated *ELODIE* and *STELIB* libraries. We find clear offset deviations between the libraries. The largest deviations are found for the *STELIB* library compared to the other two libraries, which is also the library having least stars in common with the Lick/IDS library. The deviations in offsets found between the three libraries undermine the derivation of universal offsets between the Lick/IDS and these flux-calibrated systems.

We compare the fitting functions of this work to fitting functions in the literature, namely the fitting functions of Worthey et al. (1994), Worthey & Ottaviani (1997) and Schiavon (2007). Generally we find good agreement within the rms of the residuals between the data and the fitting functions of this work. The differences found in the comparisons vary significantly from index to index and especially from one stellar parameter region to another for individual indices. However, the major differences are found in the outskirts of stellar parameter space, i.e. at the temperature and metallicity ends. This is probably due to a low number of data points in these regimes for the stellar libraries, inducing uncertainties which result in the major differences found.

In a forthcoming paper (Thomas et al. in prep.) the fitting functions of this work will be implemented in stellar population models following the techniques of Maraston (2005) and Thomas et al. (2003).

A user friendly Fortran 90 code is available online at www.icg.port.ac.uk/∼johanssj to easy the implementation of our fitting functions in population synthesis codes.

ACKNOWLEDGMENTS

We thank Patricia Sánchez-Blázquez for help with the *MILES* library. We thank Ricardo Schiavon and Rita Tojeiro for useful discussions regarding the empirical fitting method. We also thank an anonymous referee for a prompt and constructive report.

REFERENCES

Annibali F., Bressan A., Rampazzo R., Zeilinger W. W., Danese L., 2007, A&A, 463, 455

Borges A. C., Idiart T. P., de freitas Pacheco J. A., Thévenin F., 1995, AJ, 110, 2408

Brodie J. P., Strader J., Denicoló G., Beasley M. A., Cenarro A. J., Larsen S. S., Kuntschner H., Forbes D. A., 2005, AJ, 129, 2643

Bruzual G., Charlot S., 2003, MNRAS, 344, 1000

Burstein D., Faber S. M., Gaskell C. M., Krumm N., 1984, ApJ, 287, 586

Buzzoni A., Gariboldi G., Mantegazza L., 1992, AJ, 103, 1814

Buzzoni A., Mantegazza L., Gariboldi G., 1994, AJ, 107, 513

Carney B. W., 1996, PASP, 108, 900

Cenarro A. J., Gorgas J., Cardiel N., Vazdekis A., Peletier R. F., 2002, MNRAS, 329, 863

Cenarro A. J., Peletier R. F., Sánchez-Blázquez P. et al., 2007, MNRAS, 374, 664

Coelho P., Bruzual G., Charlot S., Weiss A., Barbuy B., Ferguson J. W., 2007, MNRAS, 382, 498

Davies R. L., Sadler E. M., Peletier R. F., 1993, MNRAS, 262, 650

Edvardsson B., Andersen J., Gustafsson B., Lambert D. L., Nissen P. E., Tomkin J., 1993, A&A, 275, 101

Faber S. M., Friel E. D., Burstein D., Gaskell C. M., 1985, ApJS, 57, 711

Forbes D. A., Beasley M. A., Brodie J. P., Kissler-Patig M.,2001, ApJ, 563, 143

Fuhrmann K., 1998, A&A, 338, 161

Gorgas, J., Faber S. M., Burstein D., Gonzalez J. J., Courteau S., Prosser C., 1993, ApJS, 86, 153

Gorgas J., Cardiel N., Pedraz S., González J. J., 1999 A&AS, 139, 29

Henry R. B. C., & Worthey G., 1999, PASP, 111, 919

Jones L. A., 1999, Ph.D. thesis, Univ. North carolina

Kissler-Patig M., Brodie J. P., Schroder L. L., Forbes D. A., Grillmair C. J., Huchra J. P., 1998, AJ, 115, 105

Korn A. J., Maraston C., Thomas D., 2005, A&A, 438, 685

Kuntschner H., 2000, MNRAS, 315, 184

Kuntschner H., 2001, Ap&SS, 276, 885

Kuntschner H., Davies R. L., 1998, MNRAS, 295, 29

Kuntschner H., Ziegler B.L., Sharples R. M., Worthey G., Fricke K. J., 2002, A&A, 395, 761

Le Borgne J. F., Bruzual G., Pelló R. et al., 2003, A&A, 402, 433

Lee H., Worthey G., Dotter A., 2009, AJ, 138, 1442

Leitherer C., Schaerer D., Goldader J. D. et al., 1999, ApJS, 123, 3

Maraston C., 1998, MNRAS, 300, 872

Maraston C., 2005, MNRAS, 362, 799

Maraston C., Greggio L., Renzini A., Ortolani S., Saglia R. P., Puzia T. H., Kissler-Patig M., 2003, A&A, 400, 823

Maraston C., Nieves Colmenárez L., Bender R., Thomas D., 2009, A&A, 493, 425

Milone A., Sansom A. E., Sánchez-Blázquez P., submitted, in Bruzual G. R., Charlot S., eds, Proc. IAU Symp. 262, Stellar Populations - Planning for the Next Decade.

Panter B., Jimenez R., Heavens A. F., Charlot S, 2007, MNRAS, 378, 1550

Prugniel, Ph., Soubiran C., 2001, A&A, 369, 1048

Puzia T. H., Saglia R. P., Kissler-Patig M., Maraston C., Greggio L., Renzini A., & Ortolani S., 2002, A&A, 395, 45

Puzia T. H., Kissler-Patig M., Thomas D., Maraston C., Saglia R. P., Bender R., Goudfrooij P., Hempel M., 2005, A&A, 439, 997

Rodríguez-Merino L. H., Chavez M., Bertone E., Buzzoni A., 2005, ApJ, 626, 411

Rose J. A., Bower R. G., Caldwell N., Ellis R. S., Sharples R. M., Teague P., 1994, AJ, 108, 2054

Sánchez-Blázquez P., Peletier R. F., Jiménez-Vicente J. et al., 2006, MNRAS, 371, 703

Sánchez-Blázquez P., Jablonka P., Noll S. et al., 2009, A&A, 499, 47

Schiavon R. P., 2007, ApJS, 171, 146

Thomas D., Maraston C., Bender R., 2003, MNRAS, 343, 279

Thomas D., Maraston C., Korn A., 2004, MNRAS, 351, 19

Thomas D., Maraston C., Bender R., Mendes de Oliveira C., 2005, ApJ, 621, 673

Tojeiro R., Heavens A. F., Jimenez R., Panter B., 2007, MNRAS, 381, 1252

Trager S. C., Worthey G., Faber S. M., Burstein D., Gonzalez J. J., 1998, ApJS, 116, 1

Trager S. C., Faber S. M., Worthey G., González J. J., 2000, AJ, 119, 1645

Tripicco M. J., Bell R. A., 1995, AJ, 110, 3035

Vazdekis A., 1999, ApJ, 513, 224

Vazdekis A., Casuso E., Peletier R. F., Beckman J. E., 1996, ApJS, 106, 307

Vazdekis A., Peletier R. F., Beckman J. E., Casuso E., 1997, ApJS, 111, 203

Walcher C. J., Coelho P., Gallazzi A., Charlot S., 2009, MNRAS, 398, 44

Worthey G., 1994, ApJS, 95, 107

Worthey G., 1998, PASP, 110, 888

Worthey G., Ottaviani D. L., 1997, ApJS, 111, 377

Worthey G., Faber S. M., Gonzalez J. J., 1992, ApJ, 398, 69

Worthey G, Faber S. M., Gonzalez J. J., Burstein D., 1994, ApJS, 94, 687

York D. G., Adelman J., Anderson J. E. Jr. et al., 2000, AJ, 120, 1579

APPENDIX A: FITTING FUNCTIONS FOR LICK/IDS RESOLUTION

Short version, full appendix can be found at www.icg.port.ac.uk/∼johanssj

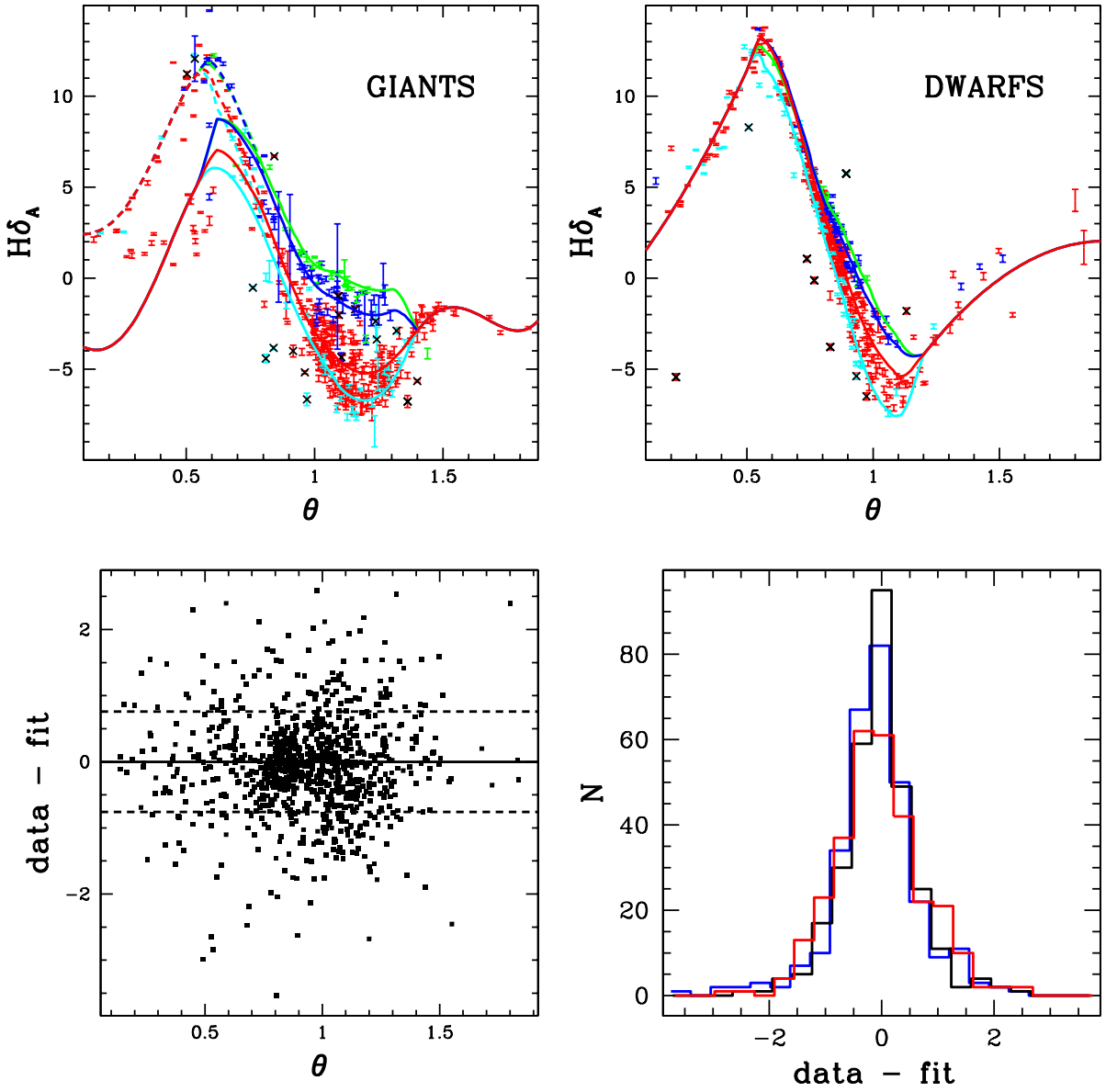

Figure A1. $H_\delta A$, same as Fig. 3. Dashed-lines for additional $\log g$-value ($\log g = 3.3$) cover the data points in strong $\log g$-dependent regions.

APPENDIX B: FITTING FUNCTIONS FOR *MILES* RESOLUTION

Short version, full appendix can be found at www.icg.port.ac.uk/∼johanssj

Table B1. *$H\delta_A$ fitting function coefficients for* MILES *resolution*

	overall rms=0.8009							
	$\log g \leqslant 4.0$ and θ limits:				$\log g \geqslant 3.6$ and θ limits:			
Term	$\leqslant 0.62$	$0.53 - 1.1$	$0.90 - 1.4$	$\geqslant 1.3$	$\leqslant 0.57$	$0.50 - 0.90$	$0.80 - 1.2$	$\geqslant 1.08$
Const.	-8.002	-136.8	36.39	-127.4	-3.369	-134.7	-49.75	-41.96
θ	-12.19	487.8	x	23.06	16.05	596.3	297.8	42.42
[Fe/H]	x	-2.367	41.22	x	x	-13.31	31.61	x
$\log g$	-4.330	21.43	2.662	x	x	x	-0.5889	x
θ^2	x	-550.1	-88.27	103.1	13.26	-922.4	-423.0	-9.752
$[\mathrm{Fe/H}]^2$	x	x	0.5080	x	x	-3.267	x	x
$\log g^2$	5.072	x	x	x	0.1957	x	x	x
θ[Fe/H]	x	x	-78.94	x	x	31.04	-68.15	x
$\theta \log g$	x	-44.24	-6.149	x	0.2840	26.90	x	x
[Fe/H]$\log g$	x	0.2318	x	x	x	x	x	x
θ^3	273.0	195.6	48.49	49.23	x	448.91	175.3	x
$[\mathrm{Fe/H}]^3$	x	0.5286	0.3213	x	x	-0.1733	-0.1461	x
$\log g^3$	-0.8813	x	x	x	x	x	x	x
θ^2[Fe/H]	x	x	34.99	x	x	-20.90	33.01	x
$\theta^2 \log g$	-16.26	22.55	3.167	x	x	-17.20	-1.042	x
$\theta[\mathrm{Fe/H}]^2$	x	1.297	x	x	x	2.919	-0.7101	x
$[\mathrm{Fe/H}]^2 \log g$	x	x	x	x	x	0.02043	x	x
$\theta \log g^2$	2.150	x	x	x	x	-1.628	x	x
θ^4	-275.2	x	x	-108.1	x	x	x	x
θ^5	x	x	x	31.52	x	x	x	x
rms	1.033	1.076	0.8149	0.6510	0.8884	0.5558	0.5954	1.477
N	96	346	359	41	49	278	276	33